Structural and electrical conduction behaviour of yttrium doped strontium titanate: anode material for SOFC application

Saurabh Singh[a], Priyanka A. Jha[a], Sabrina Presto[b], Massimo Viviani[b], A. S. K. Sinha[c], Salil Varma[d] and Prabhakar Singh[a*]

[a]*Department of Physics, Indian Institute of Technology (Banaras Hindu University) Varanasi-221005, India*

[b]*CNR-ICMATE, c/o DICCA-UNIGE, Via all'Opera Pia 15, 16145, Genova, Italy*

[c]*Department of Chemical Engineering and Technology, Indian Institute of Technology (Banaras Hindu University), Varanasi-221005, India*

[d]*Chemistry Division, Mod. Labs., Bhabha Atomic Research Centre, Trombay, Mumbai, 400085, India*

*E-mail: psingh.app@iitbhu.ac.in

Abstract

Yttrium (Y^{3+}) doped strontium titanate ($Y_xSr_{1-x}TiO_{3-\delta}$ with x = 0, 0.03, 0.05, 0.08 and 0.10) was synthesized via citrate-nitrate auto-combustion route. The electrical and structural properties of the prepared compositions were investigated to check their suitability as anode material for SOFC application. The XRD patterns of synthesized specimens showed single phase having crystal structure similar to that of the undoped $SrTiO_3$. Trace amounts of secondary phase were observed in compositions with x $\geq$ 0.05. The FESEM micrographs of all compositions revealed a non-monotonous

behaviour of grain size in $Y_xSr_{1-x}TiO_3$ system with YST8 as most porous sample among all prepared compositions. The oxygen content in the specimens was also confirmed through XPS analysis. The conductivity values in air and H_2 atmosphere were obtained from Nyquist plots in the temperature range of 100 to 700 ^{o}C. From a systematic study, the conduction mechanism was explained on the basis of defect chemistry. Moreover, the chemical stability of samples was checked through XRD patterns after the conductivity measurements in H_2 atmosphere. Results showed that amongst all the prepared samples, $Y_{0.08}Sr_{0.92}TiO_3$ may be proposed as a promising composition as anode material for SOFC application.

Keywords: Perovskite; Defects; Electrical conductivity; SOFC

1. Introduction

Fuel cells are introduced to resolve the issues of environmental pollution and energy crisis, receiving more attention in last two decades to make them efficient, cost-effective and technologically viable. Solid oxide fuel cell (SOFC) is one of the special type of fuel cell that converts chemical energy directly into electrical energy without involving the process of combustion [1,2]. These properties have made SOFC as an attractive emerging technology. The wide range of doped $SrTiO_3$ has been found as anode materials for SOFC [3-6]. In literature, several attempts have been made to use Y-doped $SrTiO_3$ with A-site deficient stoichiometry as anode in a solid oxide fuel cell for e.g. $Y_{0.07}Sr_{0.895}TiO_3$ has been utilized as anode in an electrolyte supported fuel cell [7]. Further, $Y_{0.08}Sr_{0.88}TiO_3$ was used to impregnate a backbone of YSZ electrolyte supported SOFC [8] and YST–SDC composite impregnated by Ni to act as catalyst [9].

Perovskite-type oxides (ABO_3) are promising candidates as anode for SOFCs and sensor as well due to their mixed ionic/electronic (electrical) conductivity with good catalytic activity [10, 11, 12]. Pure $SrTiO_3$ perovskite cannot be used as anode due to its low electrical conductivity, whereas donor doped $SrTiO_3$ systems are found to be suitable to anodic conditions due to their chemical and thermal stability, high electrical conductivity and carbon/sulfur tolerance [13]. It is well known that in $SrTiO_3$ based systems, the oxidation of fuel occurs at triple phase boundary region and mixed conductivity feature provides oxidizing reaction sites that decreases the polarization and accelerate the anode reaction [6]. However, the combination of ionic and electronic conductivity could not satisfy the requirements for the electrode materials, therefore, many efforts have been made to enhance the conductivity of the various materials. It is reported that the acceptor doping in the perovskite materials enhances the ionic conductivity [14, 15] whereas, the donor doping increases the electronic conductivity [6]. Several authors have reported that Yttrium acts as donor dopant for the $SrTiO_3$ system due to less difference between ionic radii of Y^{3+} (1.22 Å, CN 12) and Sr^{2+} (1.44 Å, CN 12). As the results of doping, two phenomena occur simultaneously, first maintain electro-neutrality in lattice defect structure due to charge imbalance between Y^{3+} and Sr^{2+} ions and second improve the electrical conductivity of $SrTiO_3$ *via* the formation of oxygen-rich planes. In addition to that, redox coupling between Ti^{4+} and Ti^{3+} that also occurs in the system contributes to improving the electrical conductivity under reducing atmosphere and shows an n-type semiconducting behaviour [16-19].

In the present work, a systematic investigation on Y^{3+} doped $SrTiO_3$ ($Y_xSr_{1-x}TiO_{3-\delta}$ with x = 0, 0.03, 0.05, 0.08 and 0.10) was performed and results obtained were analysed. Samples were synthesized *via* citrate-nitrate auto-combustion route using

citric acid as fuel agent and the effect of Yttrium (Y^{3+}) doping on electrical conductivity in $SrTiO_3$ under air and H_2 atmospheres was investigated through electrochemical impedance measurements.

2. Experimental

2.2 Sample preparation

The samples of the system $Y_xSr_{1-x}TiO_{3-\delta}$ with x = 0, 0.03, 0.05, 0.08 and 0.10 abbreviated as YST0, YST3, YST5, YST8 and YST10, respectively were synthesized *via* citrate-nitrate auto-combustion route. The starting materials, Y_2O_3 (99.9%), SrO (99.5%), $C_{12}H_{28}O_4Ti$ (97%) and citric acid were taken in appropriate amounts. The weighed Y_2O_3 and SrO were converted individually into Yttrium nitrate and Strontium nitrate respectively with the help of dilute nitric acid. Thereafter, all nitrates were dissolved into distilled water individually and mixed together to form clear and homogeneous solution. The weighed citric acid was also added to the solution. Another solution of titanium iso-propoxide ($C_{12}H_{28}O_4Ti$) in ethylene glycol was mixed at 100 ºC to form a homogeneous solution. Then all the solutions were dissolved in distilled water with a few drops of ammonium solution to maintain the pH value of 2. In the mixed solution, white precipitate of titanium hydroxide was formed which was dissolved by adding a few drops of nitric acid under pH value of 2. The transparent solution was slowly evaporated on a hot plate at temperature 250 ºC under continuous stirring *via* magnetic stirrer. After a few hours, it is converted into light yellow coloured gel which upon further heating converted into light brownish colour ash. The as-prepared powder was grounded by mortar and pestel. To remove the organic binders and nitrates, it was calcined in air at 1000 ºC for 10 hours in alumina crucible. The calcined powders were pelletized in 12 mm disk by a hydraulic press of 5 tons. Thereafter, pellets were sintered

in air at 1200 $^{\circ}$C for 12 hours with heating rate of 5 $^{\circ}$C/min and then cooled down to room temperature.

2.2 Characterization techniques

X-ray diffraction (XRD, Rigaku Miniflex II desktop) with Cu- Kα radiation (λ = 1.54098 Å) in 2θ range of 20° to 70° with a step size of $\Delta2\theta$ = 0.02° was used to characterize the phase structure of as sintered and post reduced $Y_xSr_{1-x}TiO_3$ samples (x=0.00, 0.03, 0.05, 0.08 and 0.10) at room temperature. The relative density of each sample was measured by Archimede's principle employing Denver SI-234 density measurement kit. Microstructure of the samples was studied by field emission scanning electron microscope (FESEM, NOVA NANOSEM 450). Average grain sizes of Y doped $SrTiO_3$ samples were statistically calculated by ImageJ software. The XPS spectra of all compositions were measured by a high performance analytical instrument (KRATOS, Amicus) using Mg target under 1.0 × 10^{-6} Pa pressure. The XPS peaks were analysed and fitted by using XPSPEAK 4.1 software. For electrical measurements, the sintered pellets were polished and coated with Ag-paste on both sides. The resultant coated samples were cured at 700 $^{\circ}$C for 20 minutes. Electrical conductivity was measured in air between room temperature and 700 $^{\circ}$C. Samples were then reduced at 700 $^{\circ}$C for 24 h under pure flowing hydrogen and electrical conductivity was measured again down to room temperature. A four-probe test (Probostat, Norecs) was employed and the impedance was measured by Frequency Response Analyzer and Potentiostat (SOLARTRON 1250+1286, Schlumberger), in the range of frequency between 1 Hz to 10^4 Hz.

3. Results and discussions

3.1 Structural studies

The XRD patterns of the sintered samples of the system $Y_xSr_{1-x}TiO_3$ (i.e. YST0, YST3, YST5, YST8 and YST10) are shown in Fig. 1 (a). To check the symmetry, Rietveld refinement was carried out using FULL PROF Suite software package with Pseudo-Voigt wave function. From the best fit, it is observed that all the samples show cubic phase with space group $Pm\bar{3}m$ (JCPDS Card Number: 86-0178). In the samples with $x \leq 0.03$ no impurity peaks are detected, while for $x \geq 0.05$, secondary phase $Y_2Ti_2O_7$ (JCPDS Card Number: 87-1849) is observed. It is also observed that the diffraction peaks shift towards higher angle as the concentration of Yttrium is increased as shown in Fig. 1 (b). In fact, the ionic radius of Y^{3+} ions is smaller than that of Sr^{2+} ions, therefore, incorporation of Y^{3+} ions on Sr sites is expected to decrease lattice parameters leading to a shift towards higher angle in XRD patterns. However, more complex incorporation mechanisms might take place (see below), with the same effect on lattice constant.

The Reference Intensity Ratio (RIR) method was used to calculate the concentration of secondary phase [19]. RIR relates the concentration of phases (X_i) in a sample with the intensity of the highest peak (I_i) of each phase, obtained by XRD through tabulated RIR_i coefficient defined as:

$$RIR_i = R_i = I_i/I_c \tag{1}$$

where I_c is the corundum intensity in 50:50 mixture with phase i. Therefore, the concentration of secondary phase, X_s, can be calculated by eq. 2:

$$X_p/X_s = I_p/I_s \cdot R_s/R_p \tag{2}$$

where p and s are referred, respectively to main and secondary phase and X_p is the concentration of the main phase. In this case, R_p and R_s are equal to 7.32 and 7.89, respectively.

X_s values, as function of $x \geq 0.03$ in $Y_xSr_{1-x}TiO_{3-\delta}$ are reported in Fig. 2 (a). It is observed that X_s increases by increasing amount of yttrium doping.

The lattice parameters of the studied systems are also plotted as a function of tolerance factor (Fig. 2 (b)). From Table 1, it is observed that the unit cell volume decreases with increase in Y content, which may be attributed to the replacement of the Sr cation by incorporation of Y^{3+} ions within the perovskite structure [20].

Fig. 2 (c) shows the variation of intensity of XRD peak with 2θ-δ (°) where δ is the angle at which maxima occurs showing diffuseness of XRD peak (110) with the compositions and observed that the diffuseness of XRD peak increases towards left with the Y^{3+} substitution in $SrTiO_3$. The increase in diffuseness is due to the formation of polarons in the matrix [21]. Microstrain and crystallite size were calculated from XRD results by using Williamson-Hall model given by [22]:

$$\beta\cos\theta = 0.9\frac{\lambda}{t} + 4\varepsilon sin\theta \tag{3}$$

where t is average crystallite size, ε is microstrain, β is full width half maxima (FWHM) at Bragg's angle (2θ) and λ being the X-ray wavelength of CuK_α ($\lambda = 1.54098$ Å). The slope of $\beta cos\theta$ vs $4sin\theta$ curve (graphs not shown here) gives the value of microstrain and intercept gives the value of crystallite size. Fig. 2(d) shows the variation of microstrain and crystallite size with the compositions. It is observed that value of

microstrain and crystallite size showed the similar trend i.e. they are maximum for YST5, whereas, the microstrain and crystallite size decreases for YST3 and YST8.

3.2 Microstructural analysis

FESEM images of fractured samples, sintered at 1200 $^{\circ}$C in air, are shown in Fig. 3 (a)-(e). YST8 sample appears the most porous among all compositions, and that finding was confirmed with the value of density measured by Archimede's method as reported in Table 1. The average grain sizes of compositions YST0, YST3, YST5, YST8 and YST10 were found to be 2.19 µm, 1.15 µm, 3.67 µm, 1.55 µm, and 3.87 µm, respectively. Along with the formation of dense grains, water-mark and lamellar features are also observed in dense micrographs as illustrated in Fig. 3 (c and e). This non-monotonous behavior of grain size and density is coherent with the crystallite size and microstrain behavior, reported in Fig. 2 (d).

3.3 XPS analysis

The oxidation states of constituent elements are analysed using X-ray Photoelectron Spectroscopy (XPS) technique. Fig. 4 (a) shows the XPS wide spectra of Y doped $SrTiO_3$ samples. The entire XPS spectrum consists of core and satellite binding energy peaks of constituent elements including C. The binding energy (BE) peaks of the constituents are marked for different doping concentrations Y ($0.0 \leq x \leq 0.10$). The C 1s peak at ~286 eV originates from external contamination or surface-absorbed CO_2. The binding energies were further calculated after calibration with respect to the C1s reference peak. The spectra revealed binding energy peaks of Sr 3d at ~134 eV, Y 3d at~157 eV, Sr 3p at ~ 269.4 eV, Ti 2p at ~ 459.4 eV, and O 1s at ~ 530.6eV. Accordingly, Sr^{2+} state is confirmed through the above mentioned peak positions. With

the increase in Y^{3+} doping content, BE values shifted to higher energy. In Fig. 4(a), a satellite peak of O (KLL) is also observed at $\sim$741.3eV [23]. Also, O 1s spectral regions are used to obtain the information regarding the presence of oxygen vacancies in the samples.

The O-1s peaks, observed for all the compositions in the spectrum, are broader and asymmetric in nature. As the peaks are broad in nature therefore they may be splitted into two peaks. These peaks can be attributed into two different types of oxygen species: lattice oxygen and adsorbed oxygen [24]. Fig. 4 (b) reveals that the sample YST5 has higher percentage of adsorbed oxygen in comparison to the lattice oxygen as illustrated in Table 1. Whereas, in all other investigated samples, percentage of lattice oxygen is more than the adsorbed oxygen.

The oxidation states of all constituent atoms of the samples have been investigated by XPS spectra. The XPS spectra for Ti 2p of YST5 sample is shown in Fig. 4 (c). The binding energies of Ti $2p_{3/2}$ and Ti $2p_{1/2}$ for the YST5 sample are 458.3 and 464.2 eV respectively as shown in Fig. 4 (c). These ions exhibit n-type semiconducting behaviour due to redox coupling of Ti^{4+}/Ti^{3+} ions and increase the electrical conductivity as reported by Fuentes et. al 2015 [25].

3.4 Impedance analysis

From spectra obtained by impedance spectroscopy, in both air and hydrogen atmosphere, the total resistance (R_t) was obtained as the intercept of depressed semi-circular arc on the real axis at low frequency. The total conductivity of the samples was calculated by applying the formula:

$$\sigma = 1/R_t \cdot l/S \tag{4}$$

where σ is the conductivity, l is the thickness of pellet and S is the surface area of the

pellet. To analyse the mechanism of conductivity, activation energy (E_a) was calculated for each regime in air as well as in reducing atmosphere by using the relation:

$$\sigma = \sigma_0/T \cdot \exp\left(-E_a/kT\right) \qquad (5)$$

where, σ_o is pre-exponential factor, E_a is the activation energy for conduction, k is the Boltzmann constant and T is the absolute temperature.
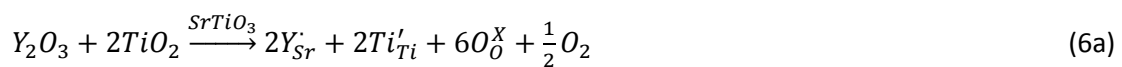
In Fig. 5 (a and b), the Arrhenius plots of log σT *vs.* 1000/T are reported for all compositions in air and hydrogen atmosphere, respectively.

It is observed that the conductivity for each composition increases passing from air to hydrogen. YST5 showed the highest conductivity in air whereas YST8 in H_2 atmosphere. All compositions showed two linear regimes in the Arrhenius plots (Fig. 5 (a) and (b)).

The activation energy calculated for all compositions is listed in Table 1. It can be noted that in air, E_a values are low for samples YST5 and YST10, suggesting electronic nature of conductivity, especially in the high temperature range.

The activation energy is further lowered after reduction in H_2 atmosphere. For all the samples, the activation energy has been found to be in the range of 0.1 to 0.2 eV except for the YST3 sample where E_a exceeds 0.5 eV.

Above reported experimental observations can be explained by considering the incorporation mechanisms of dopant into the perovskite structure of $SrTiO_3$. The average value of ionic radius for Y^{3+} in 6-fold coordination (0.90 Å) and in 12-fold coordination (1.22 Å) [26], three types of incorporation can be considered and expressed by the following equations written in the Kröger-Vink notation:

$$Y_2O_3 + 2TiO_2 \xrightarrow{SrTiO_3} 2Y_{Sr}^{\cdot} + 2Ti_{Ti}' + 6O_O^X + \tfrac{1}{2}O_2 \qquad (6a)$$

$$Y_2O_3 \xrightarrow{SrTiO_3} Y_{Sr}^{\cdot} + Y_{Ti}' + 3O_O^X \qquad (6b)$$

$$Y_2O_3 \xrightarrow{TiO_2} 2Y'_{Ti} + V^{\cdot\cdot}_O + 3O^X_O \tag{6c}$$

Eq. (6a) accounts for the incorporation of Y^{3+} at the Sr-site, with formation of positively charged defects, compensated by electrons or, equivalently, by partial reduction of Ti^{4+} to Ti^{3+}.

In the second case, eq. (6b), the incorporation takes place both at Sr- and Ti-sites, with self-compensation of charges. Finally, eq. (6c) is relevant to the case of incorporation at the Ti-site with formation of negatively charged defects, compensated by oxygen vacancies.

As already reported in case of $BaTiO_3$ [27], the most energetically favourable incorporation mechanism for Y^{3+} and similar rare-earths like Dy, Er and Gd, is the self-compensation. However, other factors can determine the actual incorporation mechanism, the most important being the amount of dopant, the cationic ratio and the temperature.

Lattice parameters and strain are determined by the incorporation mechanism so that, minimal local distorsion (microstrain) can be expected when Y^{3+} is replacing both (larger) Sr^{2+} and (smaller) Ti^{4+} atoms. The formation of the pyroclore phase also introduces point defects, namely Ti vacancies, which affect the lattice size and strain state.

Therefore, results indicate that for YST3 self-compensation (eq. 6a) is mainly active, causing limited microstrain and negligible amount of electrons leading to conduction of ionic nature due to oxygen vacancies produced either intrinsically (Schottky disorder) or through mechanism of eq. (6c).

Similar considerations hold for YST8 sample, where the small microstrain indicates simultaneous substitution at both cationic sites , which also reflect lower conductivity

and high E_a in air. In this sample, the presence of a secondary phase i.e. Ti vacancies in the main phase may account for observed lowering of the unit cell volume.

Mechanism of eq. (6a) is mainly active in samples YST5 and YST10 as demonstrated by higher conductivity, lower E_a and higher microstrain. XPS analyses are in agreement as a large amount of Ti^{3+} was detected on the surface of YST5 sample.

Under reducing atmosphere, lattice oxygen may be lost and thus oxygen vacancies will be generated as per the following equation

$$2TiO_2 \longrightarrow 2Ti'_{Ti} + V_O^{\cdot\cdot} + 3O_O^X + \frac{1}{2}O_2 \tag{7}$$

in order to conserve the electro-neutrality, the following equation must be satisfied.

$$[Ti'_{Ti}] = [Y'_{Sr}] + 2[V_O^{\cdot\cdot}] \tag{8}$$

Therefore, both extrinsic defects introduced by Y incorporation at Sr-site and intrinsic oxygen vacancies, which are formed under reducing conditions, contribute to the formation of electrons and increase of conductivity.

The conductivy of all samples is actually increased after exposure to hydrogen atmosphere; the higher value reported for sample YST8 can be attributed to the large porosity (Fig. 3 (d)) which allowed for a more efficient exchange between gas phase and solid phase. This is also suggesting that the reducing stage performed (24 h at 700 °C) was not sufficient to get equilibrium in dense samples.

3.5 Chemical stability

To check the chemical stability of the YST samples, XRD measurements were repeated after the reduction. Results are reported in Fig. 6, together with the patterns obtained after sintering in air as discussed in section 3.1. It is observed that the XRD

patterns of YST5 to YST10 (Fig. 6 (b to d)) overlap with each other showing no signs of chemical and structural degradations. Whereas, the sample YST3 (Fig. 6 (a)) showed formation of additional secondary phases after reduction. In particular, sample YST3 strongly degraded with the formation of Ti-Sr mixed oxides. Also, for all the compositions, the peaks have been shifted towards left in the reducing atmosphere showing lattice expansion. The lattice expansion might be attributed to increase of oxygen vacancies concentration under reducing atmosphere as per eq. (6c).

Among all the investigated samples, the most promising candidate for use as anodic material in SOFC is $Y_{0.08}Sr_{0.92}TiO_3$ due to its good chemical stability coupled with high conductivity and low activation energy under reducing condition.

4. Conclusions

In the present work, Y−doped $SrTiO_3$ system was studied. By changing the amount of doping element, different incorporation mechanisms are activated, particularly simultaneous incorporation of Y^{3+} at Sr- and Ti-sites or incorporation of Y^{3+} at Sr-site with electron compensation. XPS revealed the confirmation of electron compensation mechanism. Upon reduction, the conductivity increased and the activation energy decreased to nearly half in all the samples. Also, the sample YST8 was found to be chemically stable with high porosity having the highest electrical conductivity under reducing conduction. Hence, YST8 may be considered as a promising anode material for solid oxide fuel cells.

References

1. A. Choudhury, H. Chandra, A. Arora, Application of solid oxide fuel cell technology for power generation - A review. Renewable and Sustainable Energy Reviews, 20 (2013) 430-442.

2. M. Andersson, B. Sundèn, Technology review - Solid Oxide Fuel Cell. Report (2017) 359. Publisher: Energiforsk, 2017; ISBN 978-91-7673-359-2. Available online: https//energiforskmedia.blob.core.windows.net/media/22411/technology-review-solid-oxide-fuel-cell-energiforskrapport-2017-359.

3. B. C. H. Steele, A. Heinzel, Materials for fuel-cell technologies, Nature 414 (2001) 345-352.

4. H. Gu, H. Chen, L. Gao, Y. Zheng, X. Zhu, L. Guo, Oxygen reduction mechanism of $NdBaCo_2O_{5+\delta}$ cathode for intermediate temperature solid oxide fuel cells under cathodic polarization, Int. J. Hydrogen Energy, 34 (2009) 2416-2420.

5. G. Brunaccini, M. L. Faro, D. Larosa, V. Antonucci, A. S. Arico, Investigation of composite Ni-doped perovskite anode catalyst for electro-oxidation of hydrogen in solid oxide fuel cell, Int. J. Hydrogen Energy, 33 (2008) 3150-3152.

6. X. Li, H. Zhao, X. Zhou, N. Xu, Z. Xie, N. Chen, Electrical conductivity and structural stability of La-doped $SrTiO_3$ with A-site deficiency as anode materials for solid oxide fuel cells, Int. J. Hydrogen Energy, 35 (2010) 7913-7918.

7. Q. Ma, B. Iwanschitz, E. Dashjava, A. Mai, F. Tietz, H-P. Buchkremer, Electrochemical performance and stability of electrolyte-supported solid oxide fuel cells based on Y-substituted SrTiO3 ceramic anodes, Solid State Ionics, 262 (2014) 465-468.

8. A. Torabi, T. H. Etsell, Electrochemical behavior of solid oxide fuel cell anodes based on infiltration of Y-doped $SrTiO_3$, J. of Power Sources, 225 (2013) 51-59.

9. P. Puengjind, H. Muroyam, T. Matsui, K. Eguchi, Stability of solid oxide fuel cell anodes based on YST–SDC composite with Ni catalyst, J. Power Sources, 216 (2012) 409-416.

10. J. Sunarso, S. S. Hashim, N. Zhu, W. Zhou.Perovskite oxides applications in high temperature oxygen separation, solid oxide fuel cell and membrane reactor: A review, Prog. Energy Combust. Sci., 61 (2017) 57-77.

11. F. S. Silva, T. M. Souza, Novel materials for solid oxide fuel cell technologies: A literature review, Int. J. Hydrogen Energy, 42 (2017) 26020-26036.

12. M. C. Verbraeken,T. Ramos, K. Agersted, Q. Ma, C. D. Savaniu, B. R. Sudireddy, J. T. S. Irvine, P. Holtappelsb, F. Tietzc, Modified strontium titanates: from defect chemistry to SOFC anodes, RSC Adv., 5 (2015) 1168.

13. R. Moos, K. H. Hardtl, Electronic transport properties of $Sr_{1-x}La_xTiO_3$, J. Appl. Phys., 80 (1996) 393-400.

14. S. Q. Hui, A. Petric, Electrical properties of yttrium-doped strontium titanate under reducing conductions, J. Electrochem. Soc., 149 (2002) 1-10.

15. X. Li, H. Zhao, F. Gao, Z. Zhu, N. Chen, W. Shen, Synthesis and electrical properties of Co-doped $Y_{0.08}Sr_{0.92}TiO_{3-\delta}$ as a potential SOFC anode, Solid State Ionics, 179 (2008) 1588-1592.

16. S. Maletic, D. Popovic, J. Dojcilovic, Dielectric measurements, Raman scattering and surface studies of Sm-doped $SrTiO_3$ single crystal, J. Alloys Compd., 496 (2010) 388-392.

17. H. Zhao, F. Gao, X. Li, C. Zhang, Y. Zhao, Electrical properties of yttrium doped strontium titanate with A-site deficiency as potential anode materials for solid oxide fuel cells, Solid State Ionics, 180 (2009) 193-197.

18. F. Gao, H. Zhao, X. Li, Y. Cheng, X. Zhou, F. Cui, Preparation and electrical properties of yttrium-doped strontium titanate with B-site deficiency, J. Power Sources, 185 (2008) 26-31.

19. R. Snyder, The Use of Reference Intensity Ratios in X-Ray Quantitative Analysis. Powder Diffraction, 7 (4), (1992) 186-193.

20. Q. Ma, F. Tietz, D. Stöver, Nonstoichiometric Y-substituted SrTiO3 materials as anodes for solid oxide fuel cells, Solid State Ionics, 192 (2011) 535.

21. S. Shimomura, N. Wakabayashi, H. Kuwahara, Y. Tokura, X-ray diffuse scattering due to polarons in a colossal magnetoresistive manganite, Phys. Rev. Lett., 83 (1999) 4389-4392.

22. G. K. Williamson, W. H. Hall, X-ray line broadening from filed aluminium and wolfram, Acta Metall., 1 (1953) 22-31.

23. R. Pandey, P. Singh, Influence of Bi_2O_3 additive on the electrical conductivity of calcia stabilized zirconia solid electrolyte, J. Eur. Ceram. Soc., 35 (2015) 1485-1493.

24. P. Kumar, S. Presto, A. S. K. Sinha, S. Varma, M. Viviani, P. Singh, Effect of samarium (Sm^{3+}) doping on structure and electrical conductivity of double perovskite Sr_2NiMoO_6 as anode material for SOFC, J. Alloys Compd., 725 (2017) 1123-1129.

25. S. Fuentes, P. Munoz, N. Barazza, E. Chavez-Angel, C. M. Sotomayor Torres, Structural characterisation of slightly Fe-doped SrTiO3 grown via a sol-gel hydrothermal synthesis, J. Sol-Gel Sci. Technol., 75 (2015) 593-601.

26. David R. Lide, ed., CRC Handbook of Chemistry and Physics, 89th Edition (Internet Version 2009), CRC Press/Taylor and Francis, Boca Raton, FL.

27. M. T. Buscaglia, M. Viviani, V. Buscaglia, C. Bottino, P. Nanni, Incorporation of Er^{3+} into $BaTiO_3$, J. Am. Ceram. Soc., 85 (2002) 1569-1575.

Highlights

The manuscript contains the following highlights:

➢ The mechanism for conductivity was predicted by Kröger-Vink notation with the help of electron generation. This prediction was confirmed through structural measurements.

➢ The conductivity spectra were analysed through Arrhenius relation in air and H_2 atmosphere.

➢ The chemical stability of the reduced Y-doped samples was checked by XRD measurement.

➢ The conductivity data were analysed through impedance spectroscopy and concluded that 8 mol% Y-doped $SrTiO_3$ is suitable as anode material for SOFC.

Table

Table 1: Activation energy, relative density and adsorbed oxygen of YST samples

Sample	Volume (Å^3)	Relative Density (%)	Adsorbed Oxygen (%)	E_a (eV) O$_2$ atmosphere		E_a (eV) H$_2$ atmosphere	
				200-400 ºC	400-700 ºC	200-400 ºC	400-700 ºC
YST3	56.015	68	26.4	1.043	1.465	0.511	0.668
YST5	55.883	92	65.9	0.222	0.139	0.124	0.332
YST8	54.742	66	19.5	0.689	1.355	0.100	0.259
YST10	54.556	95	41.3	0.800	0.497	0.197	0.279
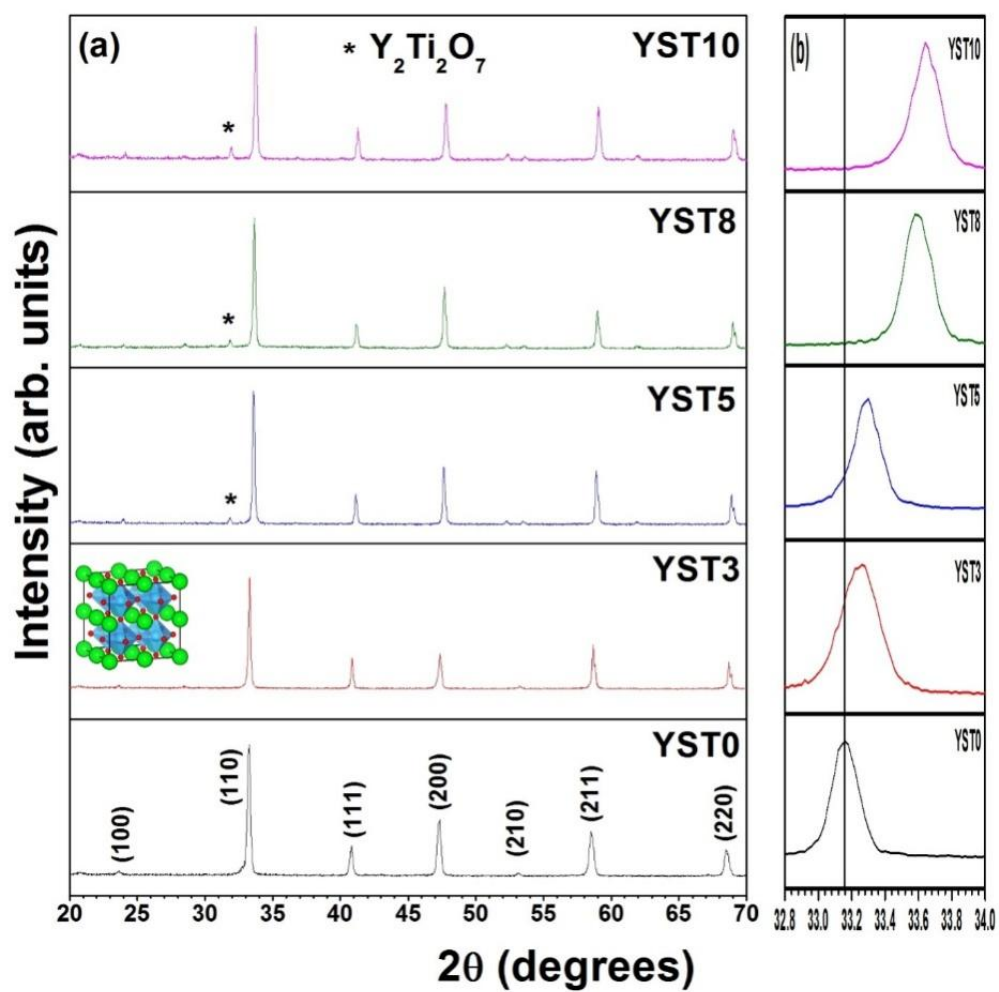
Fig. 1: (a) XRD patterns of the sintered samples of the system $Y_xSr_{1-x}TiO_3$ (i.e, YST0, YST3, YST5, YST8, and YST10) **(b)** Angle shift of (110) peak with the Y doping.
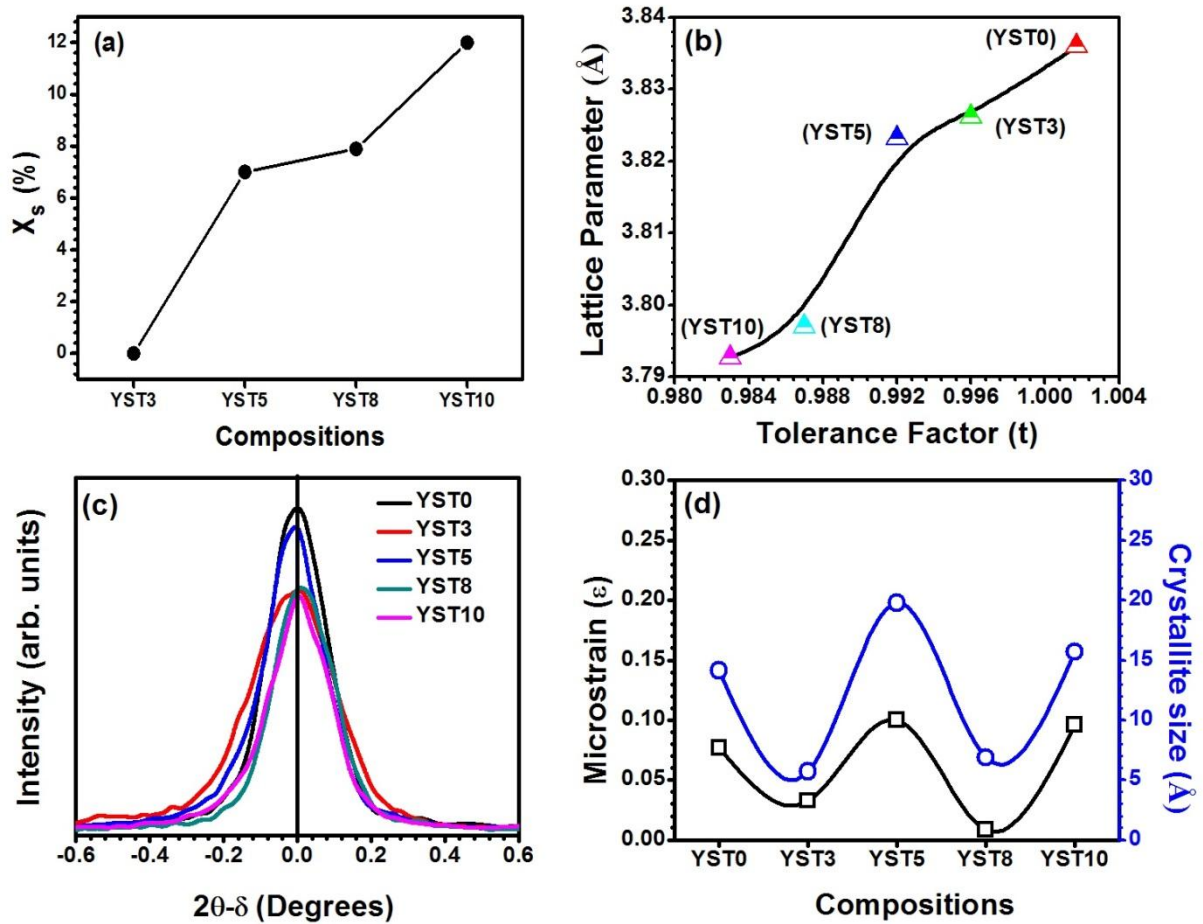
Fig. 2: (a) Secondary phase concentration, x_s, as function of $x \geq 0.03$ in $Y_xSr_{1-x}TiO_{3-\delta}$ **(b)** Variation of lattice parameter with tolerance factor, **(c)** The variation of intensity of XRD peak (110) via $2\theta\text{-}\delta$ (^{o}) with compositions (x) for $Y_xSr_{1-x}TiO_{3-\delta}$ system, and **(d)** The variation of microstrain and crystallite size with compositions (x).
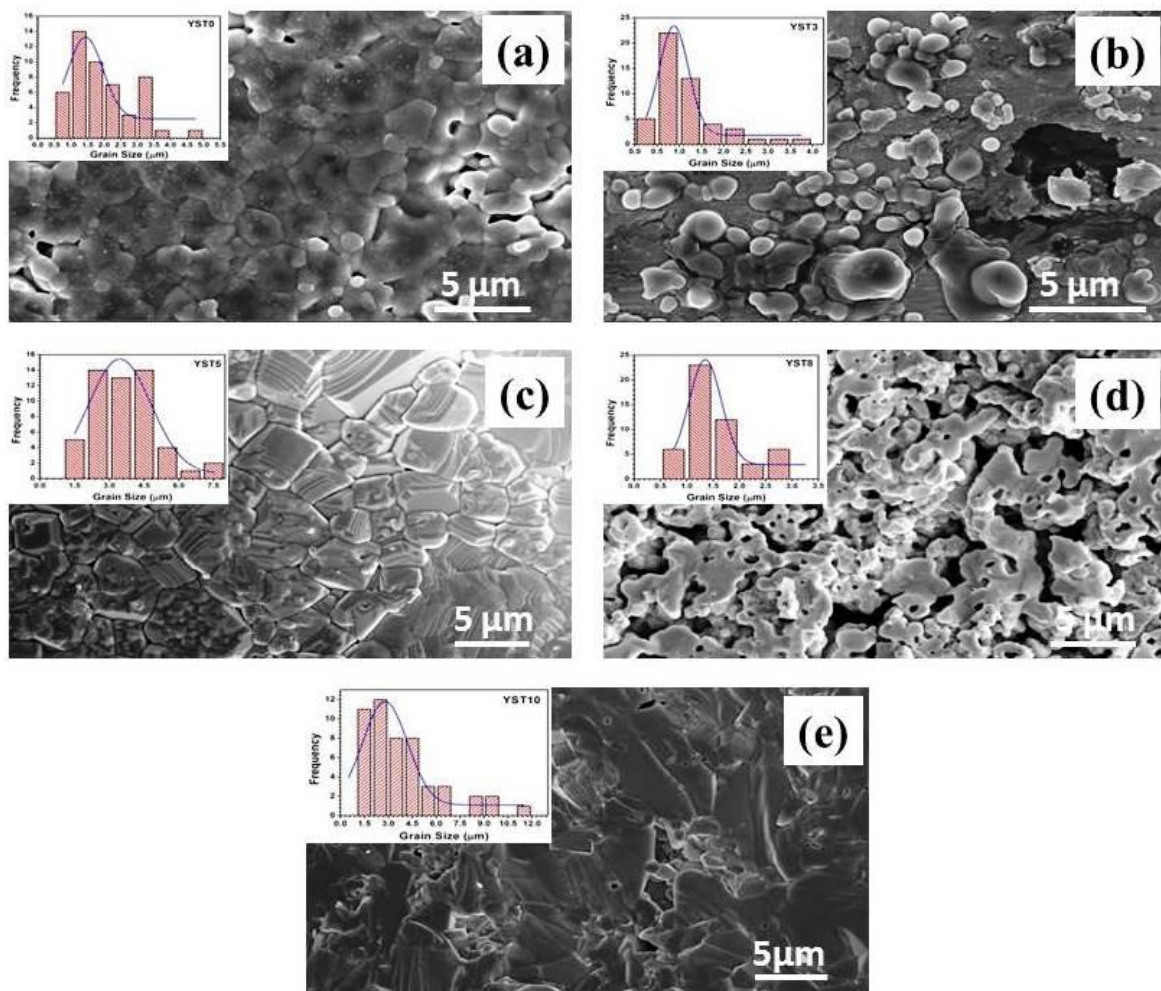
Fig. 3: FESEM images of fractured samples sintered at 1200 ^{o}C in air for **(a)** YST0 **(b)** YST3 **(c)** YST5 **(d)** YST8 and **(e)** YST10.
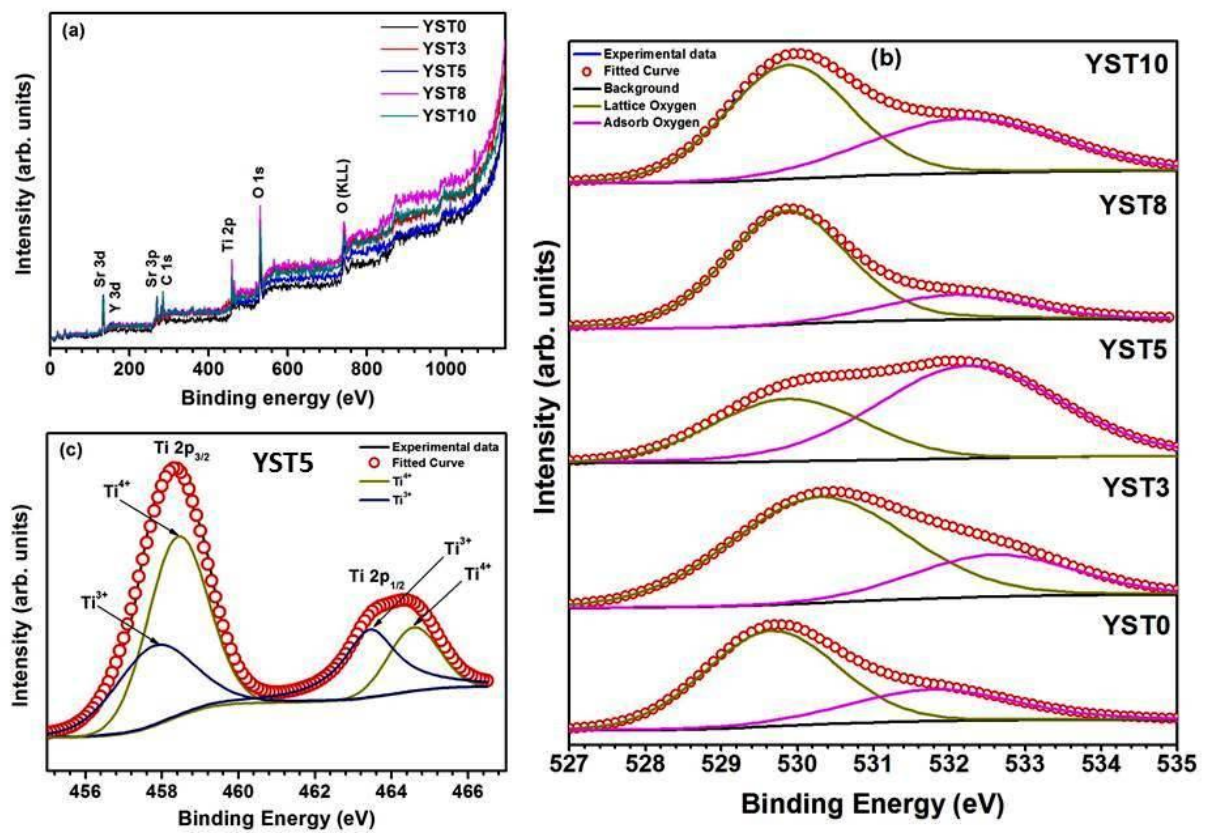
Fig. 4: (a) The XPS survey spectra of Y doped SrTiO$_3$ **(b)** The O-1s core level spectra **(c)** The XPS spectra of Ti 2p of YST5 sample.
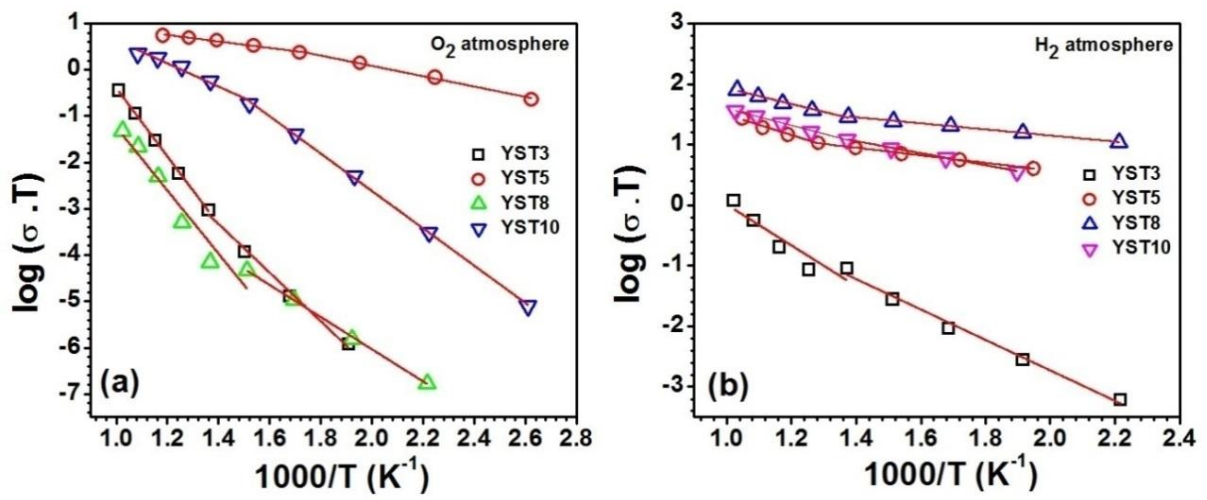
Fig. 5: The Arrhenius plot of log σT vs. 1000/T **(a)** in O_2 atmosphere **(b)** in H_2 atmosphere.
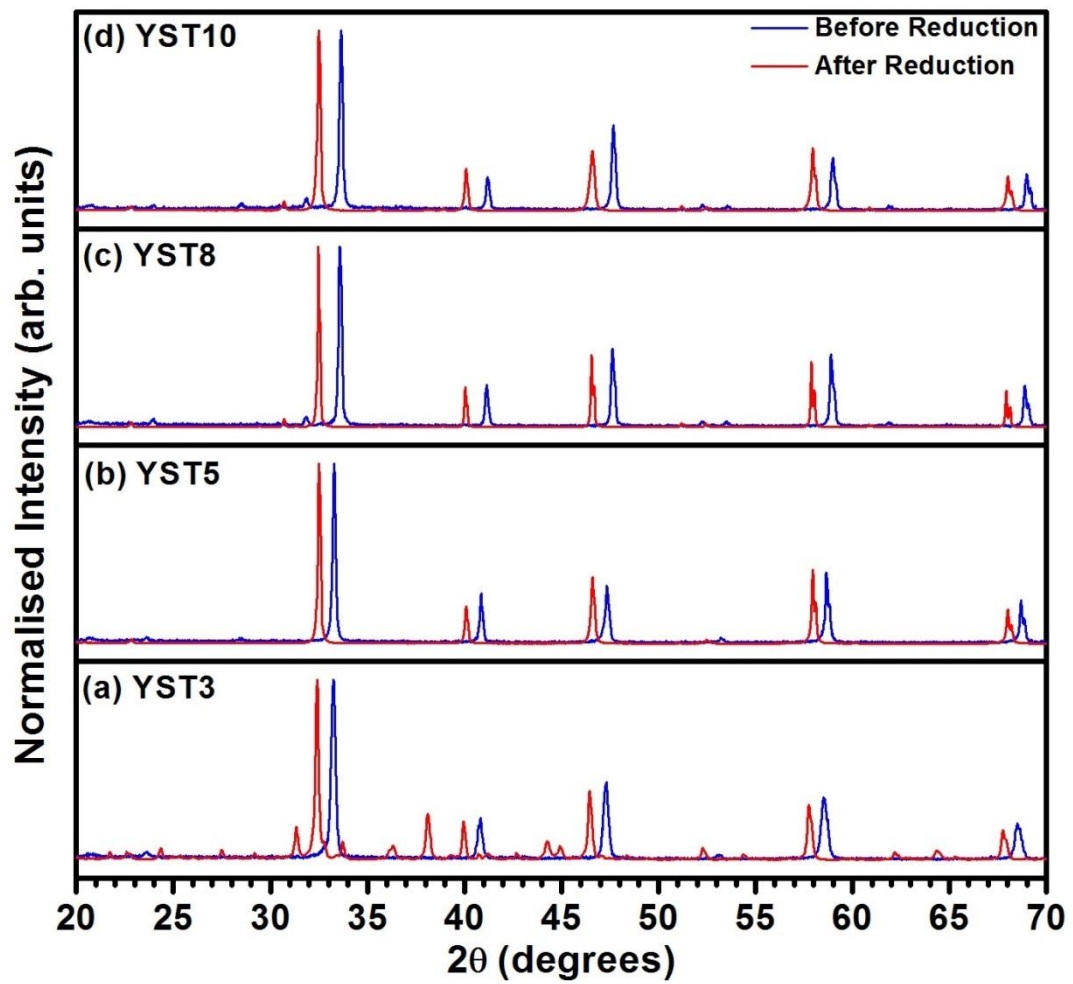
Fig. 6: XRD of **(a)** YST3, **(b)** YST5, **(c)** YST8, and **(d)** YST10 samples before and after reducing atmosphere.